nature materials

Article

https://doi.org/10.1038/s41563-024-01911-2

MXenes with ordered triatomic-layer borate polyanion terminations

Received: 8 November 2023

Accepted: 6 May 2024

Published online: 7 June 2024

Check for updates

Dongqi Li[1,12], Wenhao Zheng[2,12], Sai Manoj Gali[3,12], Kamil Sobczak[4], Michal Horák[5,6], Josef Polčák[5,6], Nikolaj Lopatik[7], Zichao Li[8], Jiaxu Zhang[1], Davood Sabaghi[1], Shengqiang Zhou[8], Paweł P. Michałowski[9], Ehrenfried Zschech[4], Eike Brunner[7], Mikołaj Donten[4], Tomáš Šikola[5,6], Mischa Bonn[2], Hai I. Wang[2,10] ✉, David Beljonne[3] ✉, Minghao Yu[1] ✉ & Xinliang Feng[1,11] ✉

Surface terminations profoundly influence the intrinsic properties of MXenes, but existing terminations are limited to monoatomic layers or simple groups, showing disordered arrangements and inferior stability. Here we present the synthesis of MXenes with triatomic-layer borate polyanion terminations (OBO terminations) through a flux-assisted eutectic molten etching approach. During the synthesis, Lewis acidic salts act as the etching agent to obtain the MXene backbone, while borax generates BO_2^- species, which cap the MXene surface with an O–B–O configuration. In contrast to conventional chlorine/oxygen-terminated Nb_2C with localized charge transport, OBO-terminated Nb_2C features band transport described by the Drude model, exhibiting a 15-fold increase in electrical conductivity and a 10-fold improvement in charge mobility at the d.c. limit. This transition is attributed to surface ordering that effectively mitigates charge carrier backscattering and trapping. Additionally, OBO terminations provide Ti_3C_2 MXene with substantially enriched Li^+-hosting sites and thereby a large charge-storage capacity of 420 mAh g^{-1}. Our findings illustrate the potential of intricate termination configurations in MXenes and their applications for (opto)electronics and energy storage.

Two-dimensional (2D) transition-metal carbides/nitrides, known as MXenes, have attracted intensive attention due to their promising applications in the areas of energy storage[1], (opto)electronics[2,3], environmental,[4,5] biomedicine[6] and future quantum technologies[6]. MXenes are characterized by the formula $M_{n+1}X_nT_x$ (n = 1–4), where M represents the transition metal, X represents carbon and/or nitrogen, and T_x represents the surface terminations. Unlike other 2D materials, MXenes typically possess a layer of functional groups (that is, T_x) capping the exposed surface metal atoms. Recent research has underscored the pivotal role of surface terminations in shaping the intrinsic properties of MXenes, such as band structures[7], electronic properties[3,8], superconductivity[9] and electrochemical functions[6]. These early results have prompted the exploration of new terminations, which offer an unparalleled and largely untapped design space for expanding the MXene family and discovering unique physicochemical properties.

MXenes are commonly synthesized via the selective removal of A-layers from layered ternary metal carbides/nitrides (that is, MAX). Although the $M_{n+1}X_n$ backbone of MXene is inherited from MAX precursors, terminations are predominantly determined by the synthetic process. Typically, wet-chemistry etching utilizing fluorine- or chlorine-containing aqueous acids yields MXenes with randomly mixed –OH, –O, –F and –Cl terminations[1]. Lewis-acid molten salt

A full list of affiliations appears at the end of the paper. ✉e-mail: wanghai@mpip-mainz.mpg.de; david.beljonne@umons.ac.be; minghao.yu@tu-dresden.de; xinliang.feng@tu-dresden.de

https://doi.org/10.1038/s41563-024-01911-2

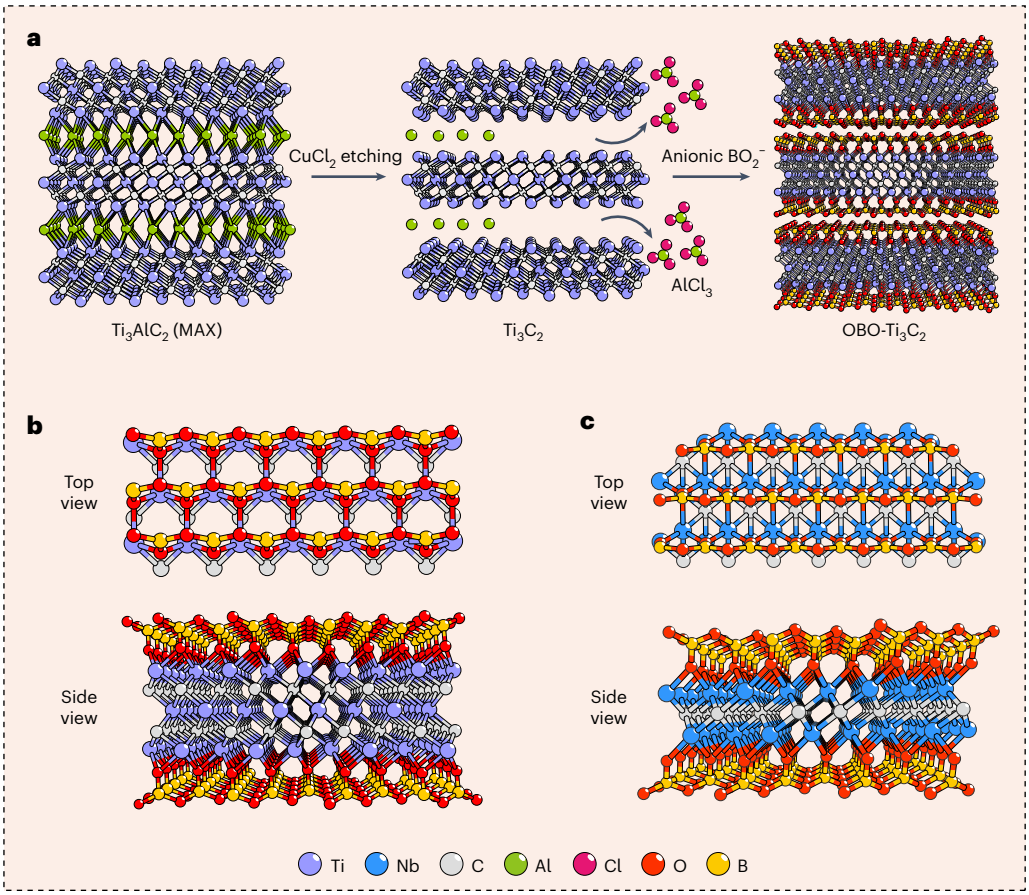

Fig. 1 | Synthesis of OBO-MXenes by the flux-assisted eutectic molten etching approach. a–c, Schematics showing the synthesis process with Ti_3C_2 MXene as an example (**a**) and atomic structures of OBO-Ti_3C_2 (**b**) and OBO-Nb_2C (**c**).

etching shows promise in producing MXenes with monoatomic-layer halogen terminations (–Cl, –Br or –I)[10–12]. These halogen terminations can be subsequently substituted with chalcogen terminations or other monoatomic-layer terminations (for example, lead and antimony) by a post-conversion process[9,13]. However, these terminations are susceptible to oxidation upon air exposure or during washing steps and thus fall short in stabilizing the ordered termination structure. Furthermore, other synthetic approaches (for example, hydrothermal etching[14,15], electrochemistry[16] and iodine-assisted etching[17]) and post-treatment strategies (for example, annealing[18] and chemical conversion[19]) offer termination manipulation, yet termination options remain constrained to the aforementioned types. Critically, the instability and disordering of the termination structure pose a major challenge for MXene applications that necessitate structural integrity and superior quality.

In this study, we showcase the synthesis of MXenes (Nb_2C and Ti_3C_2) with ordered triatomic-layer borate polyanion terminations, using a flux-assisted eutectic molten etching approach. The synthesis involves co-melting $CuCl_2$ and borax ($Na_2B_4O_7{\cdot}10H_2O$), whereupon $CuCl_2$ selectively removes aluminium layers from MAX phases, while thermally decomposed borax generates BO_2^- species that cap the MXene surface (denoted OBO terminations). Due to the ordered triatomic-layer O–B–O arrangement, terahertz (THz) spectroscopy unveils fully delocalized charge carriers of OBO-terminated Nb_2C (OBO-Nb_2C), demonstrating Drude-type band transport characteristics. This unique feature contrasts with chlorine/oxygen-terminated Nb_2C (ClO-Nb_2C) with partially localized charge transport, which leads to suppressed long-range carrier transport. Consequently, OBO-Nb_2C demonstrates a 15-fold enhancement in electrical conductivity and a 10-fold improvement in charge mobility in comparison to ClO-Nb_2C. Additionally, OBO terminations substantially increase the Li^+-hosting sites of Ti_3C_2 MXene, resulting in an ultrahigh charge storage capacity of 420 mAh g^{-1}, approximately double that of chlorine/oxygen-terminated Ti_3C_2 (ClO-Ti_3C_2, 212 mAh g^{-1}).

Synthesis of OBO-terminated MXenes

The flux-assisted eutectic molten etching approach integrates a Lewis acidic etching agent (that is, $CuCl_2$) and a polyanion supplier (that is, borax). Borax was selected for its ability to co-melt with the etching agent and to generate anionic borate species that preferentially occupy the termination positions of MXenes. Taking Ti_3AlC_2 as an illustrative example (Fig. 1a), the aluminium layers of Ti_3AlC_2 are initially removed by $CuCl_2$ during annealing through equation (1)[10]. In parallel, borax undergoes thermal decomposition, generating $NaBO_2$ and B_2O_3 through equation (2). Anionic BO_2^- species subsequently cap the Ti_3C_2 surface through equation (3), forming the terminations featured by a unique triatomic-layer O–B–O configuration (Fig. 1b). As evidenced by the calculated thermodynamic stability (Supplementary Fig. 1), BO_2^- manifests a higher affinity than Cl^- for covering the MXene surface. Finally, OBO-terminated MXenes (OBO-MXenes) are obtained following sequential washing steps involving 5 wt% HCl to remove glassy B_2O_3 and 0.1 M ammonium persulfate solution to remove copper generated during synthesis. Energy-dispersive X-ray (EDX) spectroscopy (Supplementary Fig. 2 and Supplementary Table 1) reveals that the chemical composition of OBO-Ti_3C_2 is minimally affected by the washing process. OBO-Nb_2C was synthesized through similar procedures, showing similar OBO terminations (Fig. 1c).

$$2Ti_3AlC_2 + 3CuCl_2 \rightarrow 2Ti_3C_2 + 2AlCl_3\,(g)\uparrow + 3Cu \qquad (1)$$

https://doi.org/10.1038/s41563-024-01911-2

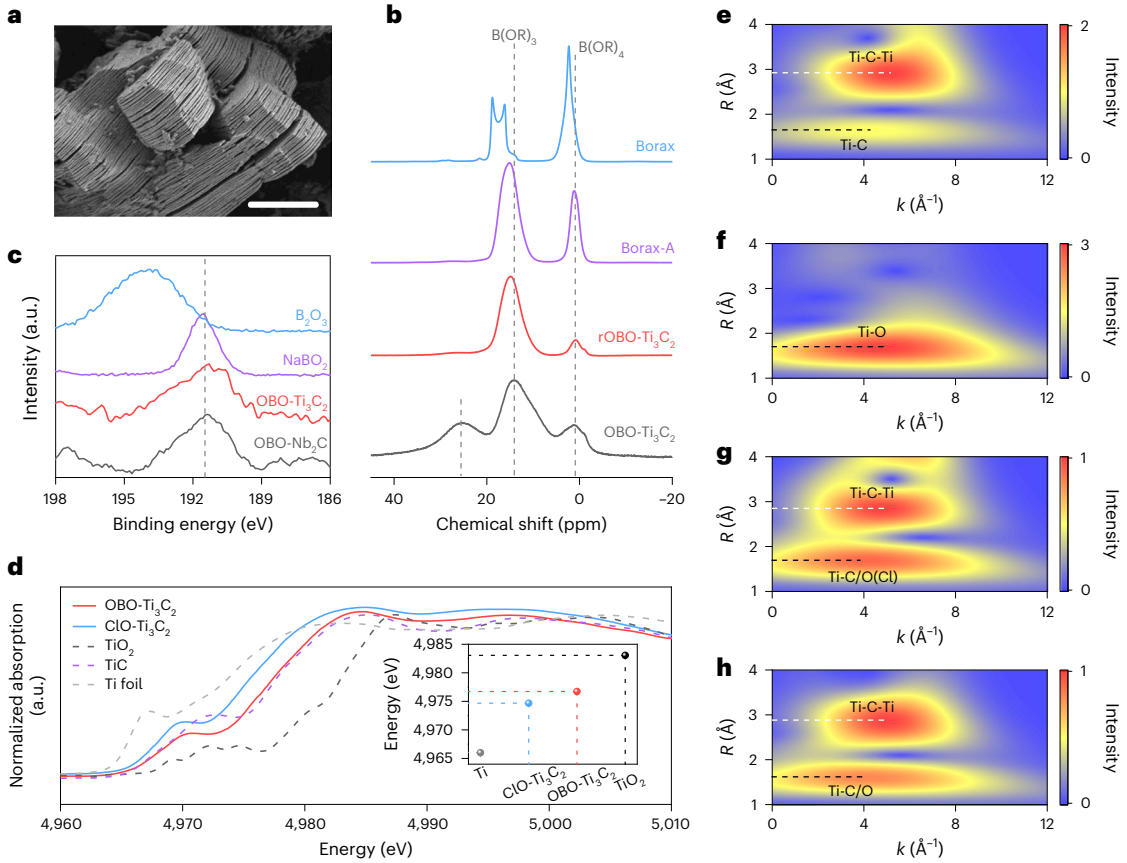

Fig. 2 | Synthesis mechanism and characterizations of OBO-MXenes. a, SEM image of OBO-Ti_3C_2. Scale bar, 2 µm. **b**, Solid-state ^{11}B MAS NMR spectra of borax, borax-A, rOBO-Ti_3C_2 and OBO-Ti_3C_2. **c**, B 1*s* XPS spectra of B_2O_3, $NaBO_2$, OBO-Ti_3C_2 and OBO-Nb_2C. **d**, XANES spectra of ClO-Ti_3C_2, OBO-Ti_3C_2 and the corresponding TiO_2, TiC and Ti foil references. Inset: comparison of corresponding edge energy (E_0) position. The E_0 values are derived for OBO-Ti_3C_2 (4,976.7 eV), ClO-Ti_3C_2 (4,974.7 eV), OBO-Nb_2C (19,001.6 eV) and ClO-Nb_2C (19,000.5 eV). **e**–**h**, Contour plots of the wavelet-transformed EXAFS of TiC (**e**), TiO_2 (**f**), ClO-Ti_3C_2 (**g**) and OBO-Ti_3C_2 (**h**).

$$Na_2B_4O_7 \rightarrow 2NaBO_2 + B_2O_3 \quad (2)$$

$$Ti_3C_2 + CuCl_2 + 2NaBO_2 \rightarrow Ti_3C_2(BO_2)_2 + 2NaCl + Cu \quad (3)$$

Scanning electron microscopy (SEM) images reveal the typical accordion-like morphology of OBO-Ti_3C_2 (Fig. 2a) and OBO-Nb_2C (Supplementary Fig. 3). Powder X-ray diffraction (PXRD) patterns reveal expanded interlayer spacings when comparing OBO-MXenes to their corresponding MAX phases (Supplementary Fig. 4). Both SEM and PXRD results substantiate the conversion from the corresponding MAX phases to the MXene phases. In addition to OBO-Ti_3C_2 and OBO-Nb_2C, we also demonstrated the applicability of the flux-assisted eutectic molten etching approach to synthesize Ti_3CN and TiNbC with OBO terminations (Supplementary Fig. 5). Moreover, OBO-MXene nanoflakes with lateral sizes of 0.5–2 µm were obtained via a liquid-phase chemical delamination (Supplementary Fig. 6).

The synthetic mechanism is supported by high-resolution solid-state ^{11}B magic-angle spinning (MAS) NMR spectra collected under a large magnetic field (18.8 T, Supplementary Fig. 7). Pristine borax was annealed under the same conditions used for MXene preparation to identify its decomposition products (borax-A). In contrast to the two characteristic ^{11}B NMR signals of borax at 2.3 and 17.4 ppm, borax-A presents two signals at 1.1 and 15.3 ppm (Fig. 2b), corresponding to the locally tetrahedrally oxygen-coordinated boron atom ($B(OR)_4$) and the threefold oxygen-coordinated boron atom ($B(OR)_3$), respectively[20]. These two signals align with those of standard B_2O_3 and $NaBO_2$ (Supplementary Fig. 7c), which verifies the thermal decomposition of borax outlined in equation (2). Moreover, the as-obtained OBO-Ti_3C_2 before washing (denoted rOBO-Ti_3C_2) exhibits a diminished ($B(OR)_4$) peak at 1.3 ppm compared with borax-A, implying the participation of $NaBO_2$ in the termination formation described in equation (3). After washing, OBO-Ti_3C_2 depicts a major signal at 14.2 ppm, which manifests the presence of OBO terminations with $B(OR)_3$-type boron atoms. The weak peak detected for OBO-Ti_3C_2 at 26.8 ppm could be attributed to the formation of a minor fraction of surface-exposed $B(OR)_3$-type boron atoms during washing (Supplementary Fig. 8). In addition, the ^{11}B MAS NMR pattern of OBO-Nb_2C (Supplementary Fig. 7d) validates the threefold oxygen-coordinated boron configuration of the OBO terminations, similar to OBO-Ti_3C_2. Fourier transform infrared spectroscopy analysis (Supplementary Fig. 9) confirms the absence of –OH groups on the surface of OBO-MXenes. In addition, high-resolution B 1*s* X-ray photoelectron spectroscopy (XPS) spectra of both OBO-Ti_3C_2 and OBO-Nb_2C (Fig. 2c) present a broad peak at 191.5 eV, matching with the binding energy of $NaBO_2$. This suggests that the boron atoms in OBO terminations have a similar electronic state to the boron atoms in $NaBO_2$, suggesting that OBO terminations originate from BO_2^- species (equation (3)). No B_2O_3 signal (194.0 eV) was observed in the B 1*s* XPS spectra of OBO-MXenes, confirming the complete removal of B_2O_3. Moreover, the C 1*s* XPS spectra of OBO-MXenes identify the characteristic carbon–metal bonding, further supporting the successful synthesis of MXenes (Supplementary Fig. 10).

https://doi.org/10.1038/s41563-024-01911-2

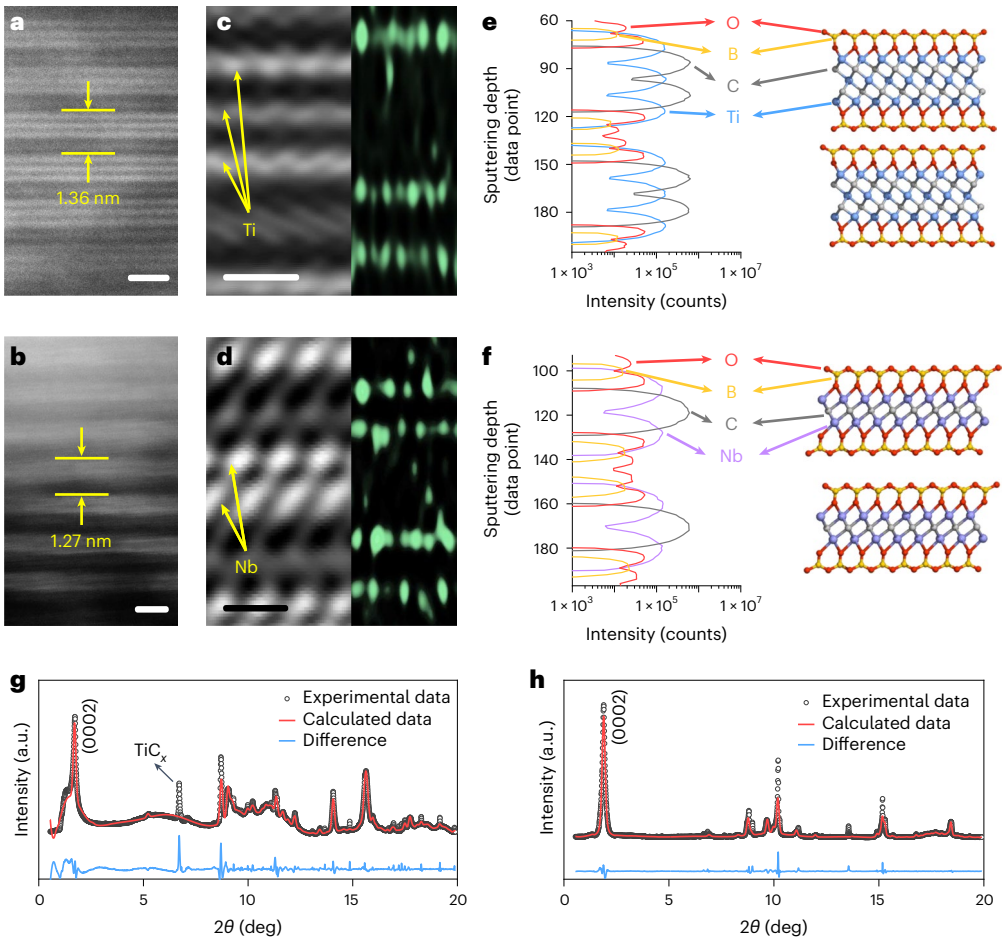

Fig. 3 | Structural characterizations of OBO-MXenes. a,**b**, Cross-sectional HAADF-STEM images of OBO-Ti_3C_2 (**a**) and OBO-Nb_2C (**b**). Scale bars, 1 nm. **c**,**d**, STEM-EDX boron-elemental mapping and corresponding HAADF-STEM images of OBO-Ti_3C_2 (**c**) and OBO-Nb_2C (**d**). Scale bars, 0.5 nm. **e**,**f**, Atomic-resolution SIMS depth profile of OBO-Ti_3C_2 (**e**) and OBO-Nb_2C (**f**). **g**,**h**, Rietveld refinement of SXRD patterns of OBO-Ti_3C_2 (**g**) and OBO-Nb_2C (**h**).

For comparison, we synthesized ClO-Ti_3C_2 and ClO-Nb_2C with mixed and disordered chlorine/oxygen terminations using a previously reported method (Supplementary Fig. 11 and Supplementary Table 2)[10]. In the metal (Ti, Nb) K-edge X-ray absorption near-edge structure (XANES) spectra, both OBO-Ti_3C_2 (Fig. 2d) and OBO-Nb_2C (Supplementary Fig. 12) present a similar spectrum shape to their corresponding metal carbide references (that is, TiC and NbC). The absorption edge energy (E_0) of OBO-MXenes is higher than that of the corresponding chlorine/oxygen-terminated MXene counterparts, which indicates that OBO terminations induce higher oxidation states in the surface metal atoms of MXenes. Additionally, metal (Ti, Nb) K-edge Fourier-transformed extended X-ray absorption fine structure (EXAFS) *R*-space spectra were performed to reveal the local coordination of metal atoms in OBO-MXenes (Supplementary Fig. 13)[21]. The visualized wavelet-transform analysis of EXAFS in *R* and *k* spaces was carried out for OBO-Ti_3C_2 (Fig. 2e–h) and OBO-Nb_2C (Supplementary Fig. 14), and the results are compared with the corresponding chlorine/oxygen-terminated MXenes, metal carbides and metal oxides. The contour intensity in the analysis revealed two maxima for both OBO-Ti_3C_2 and OBO-Nb_2C, which correspond to the first-shell metal–carbon/oxygen scattering (1.60 Å for Ti–C/O, 1.63 Å for Nb–C/O in *R* space) and second-shell metal–carbon–metal scattering (2.74 Å for Ti–C–Ti, 2.73 Å for Nb–C–Nb in *R* space). The first-shell metal–carbon/oxygen scatterings in OBO-Ti_3C_2 and OBO-Nb_2C are slightly lower in *R* space than in ClO-Ti_3C_2 (1.71 Å) and ClO-Nb_2C (1.70 Å), reflecting their relatively compact metal-termination connecting bonds.

Atomic configuration of OBO terminations

The hexagonal crystal structures of OBO-MXenes were further identified by their high-resolution transmission electron microscopy and selected area electron diffraction patterns (Supplementary Fig. 15). The homogeneous distribution of titanium/niobium, carbon, oxygen and boron throughout the MXene grain is confirmed by the EDX elemental mapping of OBO-Ti_3C_2 and OBO-Nb_2C (Supplementary Fig. 16). Neither EDX nor XPS (Supplementary Fig. 17) analyses identify any chlorine signals. Relying on the quantified EDX result (Supplementary Table 3), the formulas of OBO-Ti_3C_2 and OBO-Nb_2C are estimated as $Ti_{3.1\pm0.7}C_{2.0\pm0.5}B_{2.0\pm0.3}O_{4.0\pm1.0}$ and $Nb_{2.1\pm0.4}C_{0.9\pm0.2}B_{2.0\pm0.3}O_{4.1\pm1.0}$, respectively, closely aligning with our predicted formulas, $Ti_3C_2(BO_2)_2$ and $Nb_2C(BO_2)_2$.

Atomic-resolution cross-sectional images and EDX mapping were next performed for OBO-Ti_3C_2 and OBO-Nb_2C using high-angle annular dark-field scanning transmission electron microscopy (HAADF-STEM). The interlayer distance was deduced to be 1.36 nm for OBO-Ti_3C_2 (Fig. 3a) and 1.27 nm for OBO-Nb_2C (Fig. 3b). These values notably exceed the interlayer distance of ClO-Ti_3C_2 (1.07 nm, Supplementary Fig. 18) and ClO-Nb_2C (0.97 nm, Supplementary Fig. 19). Upon closer examination of each MXene layer, we observed distinct triatomic-layer titanium atoms in OBO-Ti_3C_2 (Fig. 3c), and diatomic-layer niobium atoms in OBO-Nb_2C (Fig. 3d), consistent with the expected MXene backbone structures. Although the precise arrangement of carbon, boron and oxygen cannot be directly discerned using HAADF-STEM, STEM-EDX mapping reveals symmetric boron layers on both sides of

https://doi.org/10.1038/s41563-024-01911-2

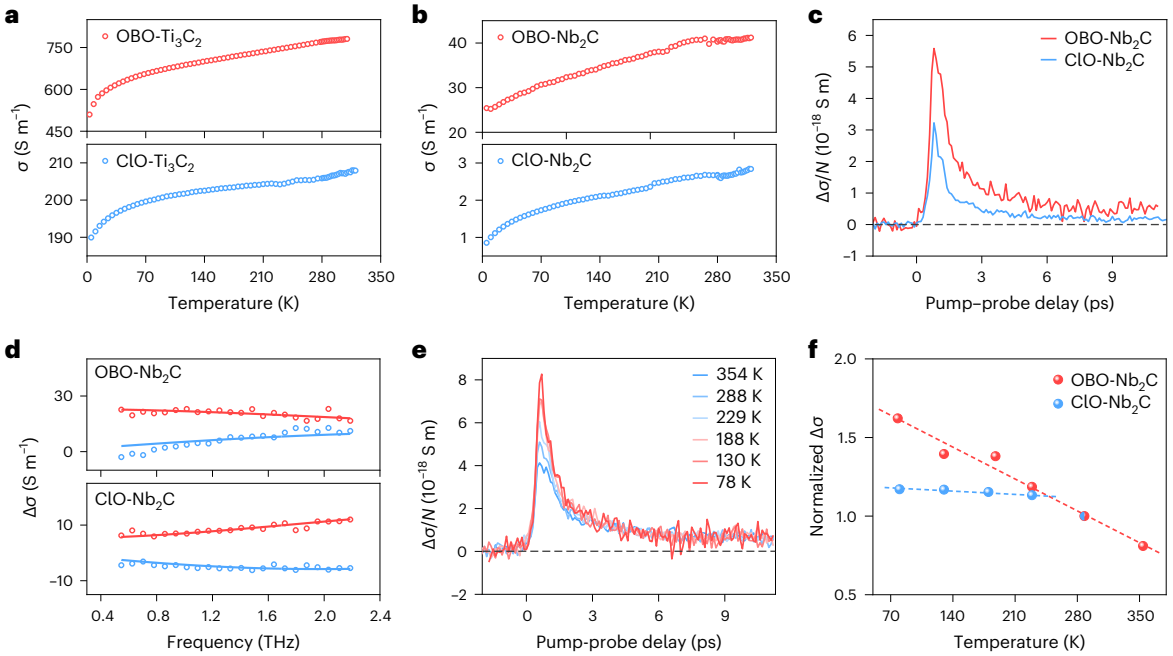

Fig. 4 | Charge-transport properties of OBO-MXenes. a,**b**, Electrical conductivity of OBO-Ti_3C_2 and ClO-Ti_3C_2 (**a**) and of OBO-Nb_2C and ClO-Nb_2C (**b**). **c**, Time-resolved THz photoconductivity ($\Delta\sigma$, proportional to the pump-induced relative changes in the transmitted field, $-\Delta E/E$) normalized to absorbed photon density N_{abs} for OBO-Nb_2C and ClO-Nb_2C. **d**, Frequency-resolved THz photoconductivity spectrum of OBO-Nb_2C and ClO-Nb_2C, recorded ~5 ps after photoexcitation. The red and blue symbols represent the real and imaginary parts of the complex-valued conductivity, respectively. The solid lines are the Drude model fitting to the OBO-Nb_2C data, and the Drude–Smith model fitting to the ClO-Nb_2C data. **e**, Temperature-dependent time-resolved THz photoconductivity of OBO-Nb_2C from 78 K to 354 K under vacuum conditions (pressure, $<1.8 \times 10^{-4}$ mbar). **f**, Temperature-dependent maximum photoconductivity normalized to the values at 288 K of OBO-Nb_2C and ClO-Nb_2C, respectively. The dashed curves are the fitted linear lines for the dot data.

each MXene layer, thereby providing evidence of the presence of boron in the terminations of both OBO-MXenes.

To elucidate the atomic configuration of the OBO terminations, we employed an optimized ultralow-energy secondary-ion mass spectrometry (SIMS) technique with atomic-depth resolution[22]. Taking OBO-Ti_3C_2 as an example (Fig. 3e), three layers of titanium atoms are evident in each MXene layer, with two layers of carbon atoms interleaved between the titanium layers. In the outermost termination layer, three distinct atom layers are observed, exhibiting an O–B–O configuration. Specifically, one oxygen layer is adjacent to the outer titanium layer, while another layer of boron is positioned in the middle, followed by an outermost layer of oxygen. The SIMS depth profile of OBO-Nb_2C indicates the same triatomic-layer configuration of OBO terminations (Fig. 3f). It should also be noted that we detected the presence of oxygen in the carbon layers of the OBO-MXene backbones (Supplementary Fig. 20), consistent with a previous report[22]. Moreover, the SIMS profiles of OBO-Ti_3C_2 before and after washing during synthesis exhibit no discernible changes in the intensity of the titanium, carbon, boron and oxygen signals. We conclude from this that the unique borate polyanion terminations form through the reconstruction of molten BO_2^- species. These cover the MXene surface with metal–oxygen bonds, and each boron atom is threefold oxygen-coordinated. Most intriguingly, the terminations comprise three atomic layers arranged in a distinctive O–B–O configuration.

Having determined the configuration of OBO terminations, the crystal structures of OBO-Ti_3C_2 and OBO-Nb_2C are simulated by density functional theory (DFT) calculations (Supplementary Fig. 21). The optimized models are correlated with the synchrotron X-ray diffraction (SXRD) patterns of OBO-Ti_3C_2 (Fig. 3g) and OBO-Nb_2C (Fig. 3h). Rietveld refinement of the structures[23] (Supplementary Table 4) gives OBO-Ti_3C_2 lattice parameters of $a = b = 3.19$ Å, $c = 27.46$ Å, and OBO-Nb_2C lattice parameters of $a = b = 3.30$ Å, $c = 25.56$ Å. These derived parameters match well with the HAADF-STEM analysis, confirming the large interlayer distance enabled by triatomic-layer OBO terminations. The presence of TiC_x in OBO-Ti_3C_2 could originate from the impurities in the Ti_3AlC_2 MAX precursor (Supplementary Fig. 22). The simulated atomic structures also reveal that the same OBO terminations have varying effects on the backbone thickness of different MXenes and on the interlayer gap space (Supplementary Fig. 23). Furthermore, OBO terminations improve the stability of MXene structures against oxidation in water and air at room temperature (Supplementary Figs. 24–26) and at elevated temperatures (Supplementary Fig. 27).

Charge-transport properties

The electrical conductivity and photoconductivity of OBO-MXenes and chlorine-/oxygen-terminated MXenes were further assessed. Temperature-dependent van der Pauw analysis revealed that the electrical conductivity of all MXene pellets increased with rising temperatures (Fig. 4a,b), indicating the predominant influence of thermally activated transport[24]. In particular, OBO-Nb_2C displays a substantially higher conductivity (40.6 S m^{-1} at 300 K) than ClO-Nb_2C (2.6 S m^{-1} at 300 K), achieving an approximately 15-fold enhancement. Meanwhile, OBO-Ti_3C_2 shows a conductivity of 777.9 S m^{-1} at 300 K, 3.8 times that of ClO-Ti_3C_2 (205.3 S m^{-1} at 300 K). Such notable improvement in conductivity underscores the pivotal role of OBO terminations in modulating the charge-transport properties of MXenes. Moreover, the termination effect appears more pronounced in Nb_2C MXene with a triatomic-layer backbone when compared with Ti_3C_2 MXene with a pentatomic-layer backbone. This finding is also supported by their simulated band structure (Supplementary Fig. 28). It should also be noted that the van der Pauw measurement of electrical conductivity encompasses intra-flake charge transport and inter-flake charge hopping and transport through grain-contact interfaces.

We further used optical pump-THz probe (OPTP) spectroscopy to understand the mechanism governing the intrinsic intra-flake charge transport of OBO-MXenes (Supplementary Fig. 29)[25]. OPTP typically

https://doi.org/10.1038/s41563-024-01911-2

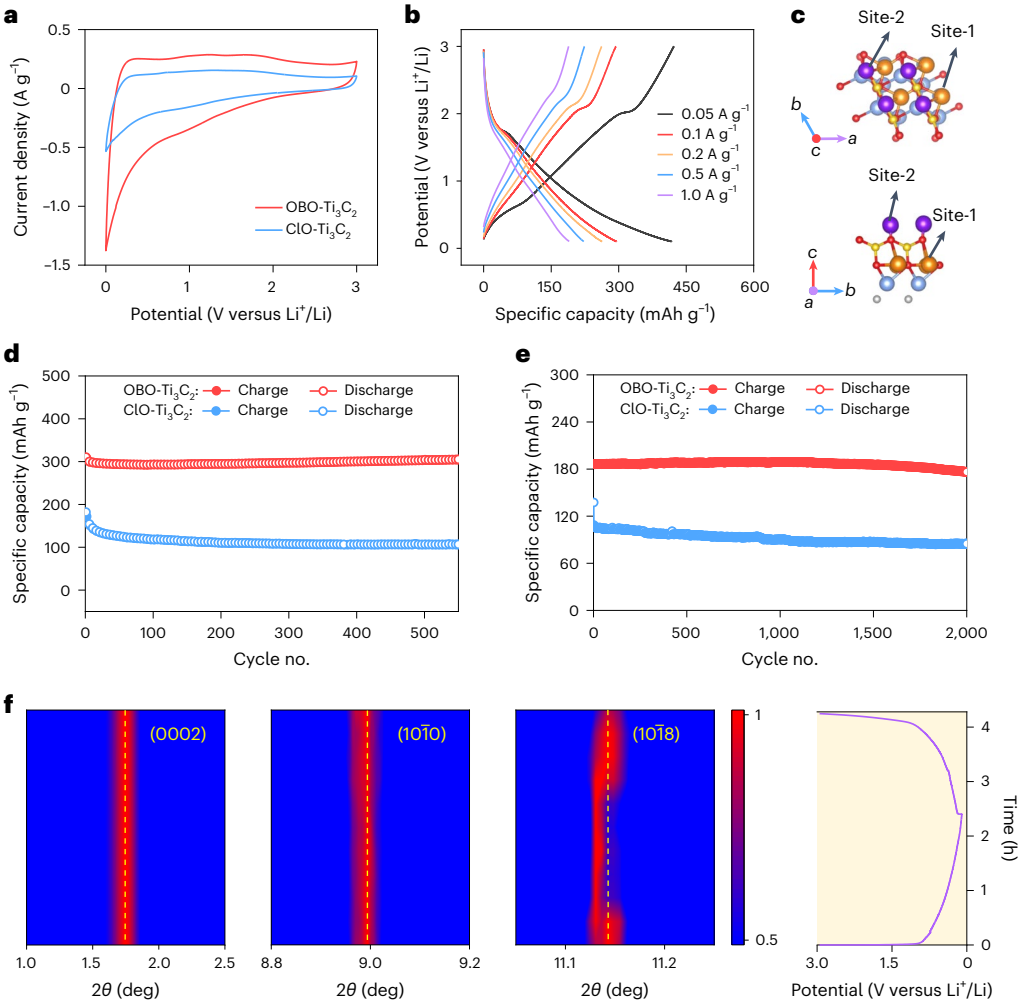

Fig. 5 | Charge-storage properties of OBO-Ti_3C_2. a, Cyclic voltammetry profiles of OBO-Ti_3C_2 and ClO-Ti_3C_2 electrodes at 0.5 mV s^{-1}. **b**, Galvanostatic charge–discharge profiles of the OBO-Ti_3C_2 electrode at various current densities. **c**, Li^+-adsorption configurations of OBO-Ti_3C_2. Blue spheres, titanium; grey spheres, carbon; yellow spheres, boron; red spheres, oxygen, purple spheres, site-1 lithium; orange spheres, site-2 lithium. **d**,**e**, Cycling stability of the OBO-Ti_3C_2 and ClO-Ti_3C_2 electrodes at 0.1 A g^{-1} (**d**) and 1 A g^{-1} (**e**). **f**, Voltage profile and contour plots of operando SXRD of the OBO-Ti_3C_2 electrode, showing a characteristic (0002) peak at 1.74°, a (10$\bar{1}$0) peak at 8.99° and a (10$\bar{1}$8) peak at 11.13°.

evaluates the short-range and intra-flake charge transport within crystalline domains on the order of tens of nanometres[3,25,26]. OPTP measurements detected a transient increase in photoconductivity ($\Delta\sigma$) for OBO-Nb_2C and ClO-Nb_2C (Fig. 4c), indicative of the generation of free carriers. Following this initial increase, a rapid photoconductivity decay was observed, presumably due to the recombination and/or trapping of the photogenerated charge carriers[3]. Importantly, the magnitude of the photoconductivity of OBO-Nb_2C is double that of ClO-Nb_2C. In the diffusive transport regime, $\Delta\sigma$ is related to the charge carrier mobility (μ) as described in equation (4), where N is the charge carrier density, φ is the photon-to-free-charge conversion quantum yield, and N_{abs} is the absorbed photon density. Assuming a similar φ, the higher photoconductivity per absorbed photon ($\Delta\sigma/N_{abs}$) of OBO-Nb_2C directly reveals its much enhanced charge mobility compared with ClO-Nb_2C. Moreover, the photoconductivity of OBO-Nb_2C decays slower than that of ClO-Nb_2C in the normalized dynamics (Supplementary Fig. 30), underscoring the slower charge-trapping rate and consequently prolonged carrier lifetime of OBO-Nb_2C.

$$\Delta\sigma = eN\mu = e\varphi N_{abs}\mu \quad (4)$$

Time-resolved THz time-domain spectroscopy (TDS) measurements were next performed to quantitatively assess charge-transport parameters[26]. Figure 4d presents the frequency-resolved, complex-valued conductivity spectra of OBO-Nb_2C and ClO-Nb_2C. Importantly, the conductivity spectrum of OBO-Nb_2C can be adequately described by the Drude model, which points to a band-transport mechanism with fully delocalized charge carriers. In contrast, ClO-Nb_2C displays a partially localized charge-transport effect, where the real conductivity increases with the frequency, and the dispersion can be fitted by Drude–Smith model. The Drude–Smith model describes charge carriers undergoing (partial or full) localization via preferential backscattering effects due to grain boundaries or structural disordering[27–29]. The disordered arrangement in surface terminations of ClO-Nb_2C MXenes could contribute to suppressing long-range charge transport and consequently hampering charge-carrier mobility[24,25]. By fitting the conductivity spectra, the charge scattering times (τ) of OBO-Nb_2C and ClO-Nb_2C were estimated to be 39 ± 3 fs and 29 ± 2 fs, respectively. Because surface terminations do not apparently alter the band dispersion of Nb_2C (Supplementary Fig. 28), the effective mass (m^*) of OBO-Nb_2C and ClO-Nb_2C can be considered similar. Following equation (5), c is introduced to signify the likelihood of charges undergoing backscattering at scattering sources, with the value ranging from 0 (equivalent to the Drude model) to −1 (100% backscattering). c is determined to be 0 for OBO-Nb_2C and −0.86 for ClO-Nb_2C. Consequently, we compare the macroscopic charge

carrier mobility (μ) at the d.c. limit for OBO-Nb_2C and conclude that the short-range carrier mobility in OBO-Nb_2C is improved tenfold compared with that in ClO-Nb_2C.

$$\mu = \frac{\tau \times e}{m^*}(1 + c) \quad (5)$$

Additionally, we conducted temperature-dependent OPTP measurements for OBO-Nb_2C (Fig. 4e) and ClO-Nb_2C (Supplementary Fig. 31). As displayed in Fig. 4f, the photoconductivity of OBO-Nb_2C exhibits a notable increase as the temperature drops from 354 to 78 K. This temperature-dependent behaviour supports the band-like transport feature of OBO-Nb_2C and underscores the critical role of the carrier-phonon scattering in dictating the charge-transport process. By contrast, ClO-Nb_2C exhibits a much less pronounced increase in photoconductivity and reaches saturation below 225 K. This again reflects the defect-dominated charge scattering in ClO-Nb_2C, particularly at low temperatures. The opposite temperature dependencies observed for the long-range electrical conductivity (Fig. 4a) and the short-range photoconductivity (Fig. 4f) suggest that intra-grain charge transport is governed by band-like behaviour, while long-range inter-grain transport occurs through hopping and thereby limits charge percolation[3].

All the above analyses reveal the considerably boosted charge-transport properties of OBO-Nb_2C in comparison with ClO-Nb_2C, highlighting the desirable effects of OBO terminations in diminishing the charge-carrier backscattering and trapping. In addition, the OPTP and time-domain spectroscopy measurements were performed for OBO-Ti_3C_2 and ClO-Ti_3C_2 (Supplementary Fig. 32). In comparison with ClO-Ti_3C_2, OBO-Ti_3C_2 achieves a 1.4-fold enhancement in photoconductivity and 2.3-fold improvement in macroscopic electron mobility, which verifies the generic effect of OBO terminations on enhancing the charge-transport properties of MXenes.

Ultrahigh Li^+-hosting capacity

MXenes, with Ti_3C_2 as the representative, have been widely studied for energy-storage applications due to their pseudocapacitive ion-intercalation mechanism[30,31]. We were thus motivated to understand the effect of OBO terminations on the charge-storage properties of Ti_3C_2. The electrochemical performance of OBO-Ti_3C_2, and of ClO-Ti_3C_2 as a control sample, was evaluated in 1 M $LiPF_6$. Figure 5a presents the cyclic voltammetry curves of OBO-Ti_3C_2 and ClO-Ti_3C_2 electrodes at 0.5 mV s^{-1} after activation. The OBO-Ti_3C_2 electrode presents a substantially larger cyclic voltammetry area than the ClO-Ti_3C_2 electrode, reflecting the much higher specific capacity of OBO-Ti_3C_2. Galvanostatic charge–discharge curves of the two electrodes at various current densities were collected to quantify the specific capacity. Both the OBO-Ti_3C_2 electrode (Fig. 5b) and the ClO-Ti_3C_2 electrode (Supplementary Fig. 33) exhibit slope-shaped profiles without apparent plateau. Of note, the OBO-Ti_3C_2 electrode delivers a maximum specific capacity of 420 mAh g^{-1} (1,512 C g^{-1}) at 50 mA g^{-1}. This value is nearly twice that of ClO-Ti_3C_2 (212 mAh g^{-1} and 763.2 C g^{-1}) and represents one of the highest specific capacities ever achieved for Ti_3C_2 MXenes (Supplementary Table 5). Even at a high current density of 1 A g^{-1}, the OBO-Ti_3C_2 electrode still delivers a large specific capacity of 202 mAh g^{-1}, highlighting its excellent rate capability. Moreover, OBO-Nb_2C also exhibits apparently higher Li^+-hosting capacities than ClO-Nb_2C (Supplementary Fig. 34).

We further sought insights into the high Li^+-hosting capability of OBO-Ti_3C_2 through DFT calculations. Specifically, we simulated the absorption of Li^+ on two different sites of OBO-Ti_3C_2 using a 2 × 2 supercell with a formula of $Ti_{3x}C_{2x}B_{2x}O_{4x}$ (x = 4, Supplementary Fig. 35). The absorption begins with the site inside the OBO cage (site-1), followed by the site located on the top of the outer oxygen layer (site-2) (Fig. 5c). As Li^+ is incrementally absorbed, we observe a change in the net partial charge transfer from lithium atoms to the MXene lattice (Supplementary Table 6). The $Ti_{3x}C_{2x}B_{2x}O_{4x}$ unit can accommodate up to 16 Li^+ ions (eight Li^+ ions on each side, Fig. 5c), corresponding to a theoretical Li^+-hosting capacity of 423.2 mAh g^{-1}, a value close to our experimental result. Ti_3C_2 models with monoatomic-layer terminations ($Ti_{3x}C_{2x}Cl_{2x}$ and $Ti_{3x}C_{2x}O_{2x}$, x = 4) were established for comparison. By contrast, the $Ti_{3x}C_{2x}Cl_{2x}$ (Supplementary Fig. 36) and $Ti_{3x}C_{2x}O_{2x}$ (Supplementary Fig. 37) units can accommodate a maximum of eight Li^+ ions (four Li^+ ions on each side), corresponding to a specific capacity of 224.6 mAh g^{-1}. When more than four Li^+ ions are adsorbed on each side of $Ti_{3x}C_{2x}Cl_{2x}$ and $Ti_{3x}C_{2x}O_{2x}$, the extra Li^+ ions enable minimal partial charge transfer with the MXene lattice (Supplementary Tables 7 and 8). The simulation result also proves that the lattice oxygen atoms (in carbon layers) of MXenes have a negligible effect on the Li^+-storage capability (Supplementary Fig. 38 and Supplementary Table 9). Additionally, Li^+ diffusion was calculated to be energetically more favourable in $Ti_{3x}C_{2x}B_{2x}O_{4x}$ (Supplementary Fig. 39) than in $Ti_{3x}C_{2x}Cl_{2x}$ and $Ti_{3x}C_{2x}O_{2x}$ (Supplementary Fig. 40), further supporting the superior Li^+-hosting capability of our developed OBO-Ti_3C_2.

In addition, OBO terminations contribute to the prolonged cycling stability of Ti_3C_2 MXene. In a cycling test at 0.1 A g^{-1} for 550 cycles (Fig. 5d), the OBO-Ti_3C_2 electrode exhibits a capacity retention of 98%, in stark contrast to the capacity retention of the ClO-Ti_3C_2 electrode (59%). Moreover, the OBO-Ti_3C_2 electrode retains 94% of its original capacity after 2,000 cycles at 1 A g^{-1}, whereas the ClO-Ti_3C_2 electrode maintains 79% of the original capacity (Fig. 5e). Operando SXRD was employed to monitor the structural evolution of OBO-Ti_3C_2 during Li^+ intercalation/deintercalation (Fig. 5f). The characteristic peaks appear unshifted for OBO-Ti_3C_2 during the electrochemical test, demonstrating its near-zero-strain characteristic. Meanwhile, B 1*s* XPS spectra suggest the good stability of OBO terminations during Li^+ intercalation/deintercalation (Supplementary Fig. 41). These results highlight the crucial role of OBO terminations in buffering the internal stress induced by Li^+ intercalation, which improves the structural stability of OBO-Ti_3C_2 given the notably boosted Li^+-hosting capability.

In conclusion, we have demonstrated the synthesis of MXenes with triatomic-layer borate polyanion terminations using borax-containing Lewis acidic molten salts. OBO termination, characterized by an ordered O–B–O configuration, enabled MXenes with vastly enhanced charge-transport and charge-storage properties. Specifically, we showcased that, compared to ClO-Nb_2C which exhibits localized charge-transport features, OBO-Nb_2C demonstrated band-transport behaviour that follows the Drude model, showing a notable 15-fold enhancement in electrical conductivity and a 10-fold improvement in charge mobility. Additionally, OBO-Ti_3C_2, which possesses considerably enriched Li^+-hosting sites, exhibited an excellent charge-storage capacity of 420 mAh g^{-1}, one of the highest values reported for a Ti_3C_2 electrode. Our study highlights the profound impact of constructing ordered terminations with complex configurations in promoting the desirable properties of MXenes, fostering their applications in (opto) electronics, energy devices and beyond.

Online content

Any methods, additional references, Nature Portfolio reporting summaries, source data, extended data, supplementary information, acknowledgements, peer review information; details of author contributions and competing interests; and statements of data and code availability are available at https://doi.org/10.1038/s41563-024-01911-2.

References

1. Anasori, B., Lukatskaya, M. R. & Gogotsi, Y. 2D metal carbides and nitrides (MXenes) for energy storage. *Nat. Rev. Mater.* **2**, 16098 (2017).
2. Zhao, T. et al. Ultrathin MXene assemblies approach the intrinsic absorption limit in the 0.5–10 THz band. *Nat. Photonics* **17**, 622–628 (2023).

3. Zheng, W. et al. Band transport by large Fröhlich polarons in MXenes. *Nat. Phys.* **18**, 544–550 (2022).
4. Liu, S. et al. Hydrogen storage in incompletely etched multilayer Ti_2CT_x at room temperature. *Nat. Nanotechnol.* **16**, 331–336 (2021).
5. Xie, X. et al. Microstructure and surface control of MXene films for water purification. *Nat. Sustain.* **2**, 856–862 (2019).
6. Mohammadi, A. V., Rosen, J. & Gogotsi, Y. The world of two-dimensional carbides and nitrides (MXenes). *Science* **372**, eabf1581 (2021).
7. Faraji, M. et al. Surface modification of titanium carbide MXene monolayers (Ti_2C and Ti_3C_2) via chalcogenide and halogenide atoms. *Phys. Chem. Chem. Phys.* **23**, 15319–15328 (2021).
8. Hart, J. L. et al. Control of MXenes' electronic properties through termination and intercalation. *Nat. Commun.* **10**, 522 (2019).
9. Kamysbayev, V. et al. Covalent surface modifications and superconductivity of two-dimensional metal carbide MXenes. *Science* **369**, 979–983 (2020).
10. Li, Y. et al. A general Lewis acidic etching route for preparing MXenes with enhanced electrochemical performance in non-aqueous electrolyte. *Nat. Mater.* **19**, 894–899 (2020).
11. Li, M. et al. Halogenated Ti_3C_2 MXenes with electrochemically active terminals for high-performance zinc ion batteries. *ACS Nano* **15**, 1077–1085 (2021).
12. Li, M. et al. Element replacement approach by reaction with Lewis acidic molten salts to synthesize nanolaminated MAX phases and MXenes. *J. Am. Chem. Soc.* **141**, 4730–4737 (2019).
13. Ding, H. et al. Chemical scissor-mediated structural editing of layered transition metal carbides. *Science* **379**, 1130–1135 (2023).
14. Wang, C. et al. HCl-based hydrothermal etching strategy toward fluoride-free MXenes. *Adv. Mater.* **33**, 2101015 (2021).
15. Li, T. et al. Fluorine-free synthesis of high-purity $Ti_3C_2T_x$ (T=OH, O) via alkali treatment. *Angew. Chemie Int. Ed.* **57**, 6115–6119 (2018).
16. Yang, S. et al. Fluoride-free synthesis of two-dimensional titanium carbide (MXene) using a binary aqueous system. *Angew. Chem. Int. Ed.* **57**, 15491–15495 (2018).
17. Shi, H. et al. Ambient-stable two-dimensional titanium carbide (MXene) enabled by iodine etching. *Angew. Chem. Int. Ed.* **60**, 8689–8693 (2021).
18. Lai, S. et al. Surface group modification and carrier transport properties of layered transition metal carbides (Ti_2CT_x, T: –OH, –F and –O). *Nanoscale* **7**, 19390–19396 (2015).
19. Saha, A. et al. Enhancing the energy storage capabilities of $Ti_3C_2T_x$ MXene electrodes by atomic surface reduction. *Adv. Funct. Mater.* **31**, 2106294 (2021).
20. Zhou, B., Sun, Z., Yao, Y. & Pan, Y. Correlations between ^{11}B NMR parameters and structural characters in borate and borosilicate minerals investigated by high-resolution MAS NMR and ab initio calculations. *Phys. Chem. Miner.* **39**, 363–372 (2012).
21. Ravel, B. & Newville, M. ATHENA, ARTEMIS, HEPHAESTUS: data analysis for X-ray absorption spectroscopy using IFEFFIT. *J. Synchrotron Radiat.* **12**, 537–541 (2005).
22. Michałowski, P. P. et al. Oxycarbide MXenes and MAX phases identification using monoatomic layer-by-layer analysis with ultralow-energy secondary-ion mass spectrometry. *Nat. Nanotechnol.* **17**, 1192–1197 (2022).
23. Toby, B. H. & Von Dreele, R. B. GSAS-II: the genesis of a modern open-source all purpose crystallography software package. *J. Appl. Crystallogr.* **46**, 544–549 (2013).
24. Halim, J. et al. Variable range hopping and thermally activated transport in molybdenum-based MXenes. *Phys. Rev. B* **98**, 104202 (2018).
25. Němec, H., Ǩuel, P. & Sundström, V. Charge transport in nanostructured materials for solar energy conversion studied by time-resolved terahertz spectroscopy. *J. Photochem. Photobiol. A* **215**, 123–139 (2010).
26. Ulbricht, R., Hendry, E., Shan, J., Heinz, T. F. & Bonn, M. Carrier dynamics in semiconductors studied with time-resolved terahertz spectroscopy. *Rev. Mod. Phys.* **83**, 543–586 (2011).
27. Dong, R. et al. High-mobility band-like charge transport in a semiconducting two-dimensional metal–organic framework. *Nat. Mater.* **17**, 1027–1032 (2018).
28. Cocker, T. L. et al. Microscopic origin of the Drude–Smith model. *Phys. Rev. B* **96**, 205439 (2017).
29. Zheng, W., Bonn, M. & Wang, H. I. Photoconductivity multiplication in semiconducting few-layer $MoTe_2$. *Nano Lett.* **20**, 5807–5813 (2020).
30. Wang, X. et al. Influences from solvents on charge storage in titanium carbide MXenes. *Nat. Energy* **4**, 241–248 (2019).
31. Wang, D. et al. Direct synthesis and chemical vapor deposition of 2D carbide and nitride MXenes. *Science* **379**, 1242–1247 (2023).

[1]Faculty of Chemistry and Food Chemistry & Center for Advancing Electronics Dresden (cfaed), Technische Universität Dresden, Dresden, Germany. [2]Max Planck Institute for Polymer Research, Mainz, Germany. [3]Laboratory for Chemistry of Novel Materials, Materials Research Institute, University of Mons, Mons, Belgium. [4]Faculty of Chemistry, Biological and Chemical Research Centre, University of Warsaw, Warsaw, Poland. [5]CEITEC BUT, Brno University of Technology, Brno, Czech Republic. [6]Faculty of Mechanical Engineering, Institute of Physical Engineering, Brno University of Technology, Brno, Czech Republic. [7]Chair of Bioanalytical Chemistry, Faculty of Chemistry and Food Chemistry, Technische Universität Dresden, Dresden, Germany. [8]Institute of Ion Beam Physics and Materials Research, Helmholtz-Zentrum Dresden-Rossendorf, Dresden, Germany. [9]Łukasiewicz Research Network—Institute of Microelectronics and Photonics, Warsaw, Poland. [10]Nanophotonics, Debye Institute for Nanomaterials Science, Utrecht University, Utrecht, The Netherlands. [11]Max Planck Institute of Microstructure Physics, Halle (Saale), Germany. [12]These authors contributed equally: Dongqi Li, Wenhao Zheng, Sai Manoj Gali. ✉e-mail: wanghai@mpip-mainz.mpg.de; david.beljonne@umons.ac.be; minghao.yu@tu-dresden.de; xinliang.feng@tu-dresden.de

Methods

Chemicals

Ti_3AlC_2 and Nb_2AlC MAX phases were purchased from Carbon-Ukraine. Ti_3AlCN and TiNbAlC MAX phase were purchased from Jilin 11 Technology. Borax ($Na_2B_4O_7{\cdot}10H_2O$), $CuCl_2$, NaCl, KCl, $NaBO_2{\cdot}4H_2O$, B_2O_3, $(NH_4)_2S_2O_8$, HCl (aq.), 2.5 M *n*-butyllithium solution in hexane, *N*-methyl-2-pyrrolidone (NMP), cellulose, polytetrafluoroethylene, 1 M $LiPF_6$ in ethylene carbonate and diethyl carbonate (EC/DEC, 1:1 vol%, battery grade) were purchased from Sigma-Aldrich. Hexane, tetrahydrofuran, Super P carbon black and lithium foil (purity, 99.9%; thickness, 0.75 mm) were bought from Alfa Aesar. Glass microfibre (grade GF/A) was purchased from Whatman. All chemicals were used directly without any purification.

Synthesis of OBO-MXenes

MAX phase (Ti_3AlC_2, Nb_2AlC, Ti_3AlCN and TiNbAlC), $CuCl_2$, $Na_2B_4O_7{\cdot}10H_2O$, NaCl and KCl were mixed in a molar ratio of 1:3:2:2:2 and ground in a mortar for 10 min. The mixture was then placed in a corundum boat and transferred to a tightly sealed tube furnace with an argon flow (100 sccm). The synthesis reactions of OBO-Ti_3C_2, OBO-Nb_2C and OBO-Ti_3CN MXenes were carried out at 800, 750 and 800 °C, respectively, with a heating rate of 3 °C min^{-1} and held for 24 h. The synthesis of OBO-TiNbC was performed at 700 °C with a heating rate of 3 °C min^{-1} and held for 8 h. Afterward, the product was immersed in 5 wt% HCl solution and sonicated for 30 min to remove by-products (for example, B_2O_3). The product was then washed with a 0.1 M ammonium persulfate solution to eliminate the copper particles produced. The obtained product was further washed with deionized water and ethanol before being dried in a vacuum oven for 24 h. As control samples, chlorine-/oxygen-terminated MXenes were prepared by a similar procedure, but without the addition of borax.

The delamination of OBO-MXenes was conducted by a modified chemical exfoliation approach[32]. Specifically, 50 mg of OBO-Ti_3C_2 was added to 1 ml of 2.5 M *n*-butyllithium solution in an argon-filled glovebox (H_2O and O_2 content maintained below 0.1 ppm). The sample vial was then sealed and stirred at room temperature for 24 h, followed by washing with high-purity hexane and tetrahydrofuran. Subsequently, the sample was added to 10 ml of anhydrous NMP in a centrifuge tube. After ice-water bath sonication (<5 °C) for 40 min, the supernatant with exfoliated nanoflakes was collected by centrifugation at 360*g* for 20 min to remove precipitated particles. Next, the supernatant was centrifuged at 13,000*g* for 15 min to precipitate MXene nanoflakes. Finally, the precipitated MXene nanoflakes were dispersed in anhydrous NMP.

Characterizations

XPS was performed with an Axis Supra spectrometer (Kratos Analytical). The high-resolution spectra were acquired using Al Kα X-ray radiation at an emission angle of 0° relative to the surface normal, and a pass energy of 20 eV was utilized to obtain the high-resolution spectra. Powder MXene samples were fixed on a copper adhesive tape, and all analyses were performed using a charge neutralizer system to compensate sample charging. Spectra were calibrated on a binding energy scale to the position of the C 1*s* C–C bond at 284.8 eV. Solid-state ^{11}B NMR spectra were acquired on 300 MHz (7.05 T) and 800 MHz (18.8 T) Bruker Ascend spectrometers. Measurements with the 300 MHz spectrometer were performed using a commercial 2.5 mm H-X MAS NMR probe (Bruker Biospin) at 15 kHz sample spinning rate. Measurements with the 800 MHz spectrometer were obtained using a 1.3 mm H-X MAS probe at 50 kHz spinning rate. ^{11}B MAS NMR spectra were recorded by direct excitation with a delay of 3 s between subsequent scans. Spectra were referenced using boric acid as reference for ^{11}B. PXRD was measured with an AERIS XRD system (PANalytical) with a Cu Kα source diffractometer, a scan step of 0.02° and a scan range between 5° and 70°. Fourier transform infrared spectra were measured with a Shimadzu IRSpirit spectrometer. SEM images were collected using a Zeiss Gemini S4 500. Atomic force microscopy images were collected using a Park NX10 microscope. Transmission electron microscopy investigations were conducted using a Talos F200X transmission microscope at 200 kV and a Scientific Titan Themis (ThermoFisher). Measurements were performed in STEM modes using a HAADF. EDX was used to map the chemical composition. Thermogravimetric analysis was performed with a Simultaneous Thermal Analysis DSC/TG 111 system (Setaram) from room temperature to 1,000 °C in air. SIMS experiments were conducted using a CAMECA IMS SC Ultra instrument equipped with a Cs^+ primary-ion beam operating at a high incident angle of 75° relative to the sample surface[22]. The primary-ion beam was characterized by ultralow impact energy (100 eV), moderate intensity (6 nA) and a standard diameter of 30 μm. Negative detector polarity was used for the measurements. Initially, the experimental procedure involved the utilization of a beam of primary Cs^+ ions in a parallel configuration, serving the purpose of delicately removing any potential impurity species present on the crystal surface and promoting the formation of flat surfaces. Subsequently, low-energy Cs^+ ions were directed towards the sample surface at a high incident angle, enabling selective interactions exclusively with the uppermost atomic layer. As a result of the bombardment of the sample surface by the primary Cs^+ ions, atoms from the material were sputtered away and subsequently detected as secondary ions.

Synchrotron X-ray absorption spectroscopy (XAS) was performed at beamline P65 at the PETRA III synchrotron (DESY, Hamburg, Germany). XAS data were collected in transmission mode at room temperature with energy around the Ti K-edge (4,966 eV) and the Nb K-edge (18,986 eV). The incident, transmitted and reference X-ray intensities were monitored using gas ionization chambers. A titanium/niobium foil standard served as a reference for energy calibration and was concurrently measured with the experimental samples. Prior to measurement, all powder samples were prepared as pellets (diameter, 8 mm), diluted with an appropriate quantity of cellulose, and sealed in Kapton tape within a glovebox. The collected XANES and EXAFS data were further integrated and corrected using Athena software v.0.9.26 (ref. 21). The wavelet transform of the EXAFS patterns was performed using HAMA Fortran software. To derive the EXAFS oscillations, $\chi(k)$ (k-weights, 2) was extracted as a function of photoelectron wave number k, within a selected calculation range of 0–6 Å ($R_{min} = 0$, $R_{max} = 6$). The Morlet function was used as the mother wavelet function, with parameters set to kappaMorlet = 10 and sigmaMorlet = 1.

SXRD data were collected at beamline BL04 of the ALBA synchrotron station, with 35 keV energy, $\lambda = 0.4142$ Å, and the high-angular-resolution multicrystal analyser detector set-up. To enable the operando electrochemical test, the MXene electrodes were prepared by combining MXene powder, Super P and polytetrafluoroethylene in an 8:1:1 weight ratio, assisted by ethanol. The resulting mixture was compressed into a film and subsequently dried at 80 °C for 12 h under vacuum conditions, leading to the formation of a free-standing film. A 3032-coin cell was assembled in argon-filled glovebox by utilizing the free-standing MXene electrodes as the working electrode, lithium foil as the counterelectrode, a layer of glass microfibre as the separator, and 1 M $LiPF_6$ in EC/DEC as the electrolyte. To enable X-rays to pass through, a window 5 mm in diameter was created in the middle of the coin cell shell and the lithium foil. The assembled batteries were mounted on a specialized set-up provided by the beam station for testing. The charging and discharging processes were carried out using a Biologic VMP3 potentiostat at a current density of 0.1 A g^{-1}. GSAS-II software was used to process the Rietveld refinement of the obtained SXRD patterns to derive the lattice parameters[23].

Van der Pauw measurements

The electrical conductivity of the MXenes was measured using a commercial Lakeshore Hall System (9700A). Powder MXene samples were compressed under a force of 8 tonnes to create MXene pellets with a

diameter of 8 mm and a thickness of 200 µm. Conductive silver paste was applied to establish contact between the silver wires and the pellet. Current–voltage (I–V) curves were obtained at different temperatures using a van der Pauw pattern to ensure the contacts are ohmic. The sheet resistance (R_s) of the pellet in the temperature range of 5–320 K was determined to calculate the bulk electrical resistivity (ρ) and electrical conductivity (σ).

THz spectroscopy

THz spectroscopy used a commercial regeneratively amplified and mode-locked titanium:sapphire femtosecond laser system (Spectra Physics Spitfire Ace, seeded by Mai Tai and pumped by Empower). The laser system generated pulses of approximately 50 fs duration, centred at a wavelength of 800 nm, and operated at a repetition rate of 1 kHz. THz radiation was produced through optical rectification using a non-linear zinc telluride (ZnTe) crystal oriented along the (110) direction. The resulting THz electric field was measured using a second ZnTe detection crystal via the electro-optical effect, which was probed with an 800 nm sampling pulse. The use of a ZnTe crystal enabled the measurement of frequency information in the range of 0.4–2.5 THz. For OPTP measurements, the THz absorption induced by charge carriers due to optical excitations (800 nm) was monitored by fixing the sampling beam to the peak of the THz field. Using this set-up, we measured time-dependent, pump-induced THz absorption by adjusting the time delay between the pump and THz probe. To prevent THz absorption by vapours, the entire THz set-up was maintained under a nitrogen purge. During measurements, the samples were either purged with dry nitrogen or placed under vacuum conditions ($<2\times10^{-4}$ mbar). Charge carriers were photogenerated in MXene samples using an optical pump pulse (1.55 eV laser pulse with ~50 fs duration), and subsequently probed using a single-cycle THz pulse with a frequency bandwidth of 2 THz. The time-resolved photoconductive response ($\Delta\sigma$) of charge carriers was monitored by characterizing the time-dependent pump-induced THz absorption (ΔE) using the thin-film approximation, by using equation (6), where $Z_0 = 377\ \Omega$ is the impedance of free space, l is excitation thickness and $n_{sub} = 1.95$ is the refractive index of the fused silica substrate in the THz range. E_{pump} and E_0 represent the peak intensity of the transmitted THz field with and without photoexcitation ($\Delta\sigma = \sigma_{pump} - \sigma_0$), respectively.

$$\Delta\sigma = -\frac{n_{sub}+1}{Z_0 l} \times \frac{E_{pump}-E_0}{E_0} \quad (6)$$

Extraction of frequency-resolved photoconductivity

THz time-domain spectroscopic measurements were conducted with a fixed pump–probe delay time. The entire THz waveform transmitted through the sample without photoexcitation was set as the reference (E), and we measured the photoinduced THz waveform modulation $\Delta E = E_{pump} - E$ in the time domain. We utilized Fourier transformation to convert the relative change of THz transmission from the time domain to the frequency domain. Subsequently, we applied the thin-film approximation to quantify the complex photoconductivity spectra.

Electrochemical measurements

The MXene electrodes were prepared by mixing the MXene powder (80 wt%) with 10 wt% Super P and 10 wt% CMC binder to form a slurry. Subsequently, the electrode was prepared by dispersing the mixture in distilled water and coated onto a copper foil by a typical blade method. After drying in a vacuum oven for 24 h at 50 °C, 8-mm-diameter discs were cut and used as the working electrodes. The loading mass of MXene was 1 ± 0.1 mg cm^{-2}. CR2025 coin cells were further assembled in an argon-filled glovebox with H_2O and O_2 content less than 0.1 ppm, using the MXene electrodes as the working electrode, lithium foil (diameter, 8 mm) as the counterelectrode, a layer of glass microfibre as the separator and 1 M $LiPF_6$ in EC/DEC as the electrolyte. Galvanostatic charge–discharge measurements were conducted on a LAND CT2001A battery test system, while cyclic voltammetry was performed by using a Biologic VMP3 potentiostat. Both OBO-Ti_3C_2 and ClO-Ti_3C_2 electrodes needed an activation process with charge and discharge cycling at 0.1 A g^{-1}.

Computational studies

DFT calculations were performed using the projector-augmented wave basis set, as implemented in the VASP code[33,34]. Exchange and correlation effects were treated at the Perdew–Burke–Ernzerhof level of theory and the dispersion forces by the Grimme correction (Perdew–Burke–Ernzerhof + D2)[35,36]. A kinetic energy cut-off of 600 eV was implemented, using a Monkhorst–Pack sampling of 4 × 4 × 1 for monolayers and 4 × 4 × 4 for bulk MXene samples for the Brillouin zone integration during all geometry optimizations. The self-consistent field convergence criterion was set to 10^{-5} eV, and the ionic relaxation was stopped when the change of the total free energy was $<10^{-4}$ eV between two subsequent steps. For MXenes without and with Li^+ adsorbed on the MXene surface, vacuum spacing was set to 30 Å to avoid any interaction with periodic images. Subsequent self-consistent field calculations were performed using a denser k-point grid of 6 × 6 × 1 for monolayers and 6 × 6 × 6 for bulk samples for the Brillouin zone integration. Partial charge-transfer analysis was performed using the DDEC06 method[37]. Li^+ diffusion on the MXene surface was computed using the climbing image–nudged elastic band method implemented in the VASP code[38,39].

Data availability

All data are available in the main text or the Supplementary Information. Source data are provided with this paper.

References

32. Zhou, C. et al. Hybrid organic–inorganic two-dimensional metal carbide MXenes with amido- and imido-terminated surfaces. *Nat. Chem.* **15**, 1722–1729 (2023).
33. Kresse, G. & Furthmüller, J. Efficient iterative schemes for ab initio total-energy calculations using a plane-wave basis set. *Phys. Rev. B* **54**, 11169–11186 (1996).
34. Kresse, G. & Joubert, D. From ultrasoft pseudopotentials to the projector augmented-wave method. *Phys. Rev. B* **59**, 1758–1775 (1999).
35. Perdew, J. P., Burke, K. & Ernzerhof, M. Generalized gradient approximation made simple. *Phys. Rev. Lett.* **77**, 3865–3868 (1996).
36. Grimme, S. Semiempirical GGA-type density functional constructed with a long-range dispersion correction. *J. Comput. Chem.* **27**, 1787–1799 (2006).
37. Limas, N. G. & Manz, T. A. Introducing DDEC6 atomic population analysis: part 4. Efficient parallel computation of net atomic charges, atomic spin moments, bond orders, and more. *RSC Adv.* **8**, 2678–2707 (2018).
38. Henkelman, G. & Jónsson, H. Improved tangent estimate in the nudged elastic band method for finding minimum energy paths and saddle points. *J. Chem. Phys.* **113**, 9978–9985 (2000).
39. Henkelman, G., Uberuaga, B. P. & Jónsson, H. A climbing image nudged elastic band method for finding saddle points and minimum energy paths. *J. Chem. Phys.* **113**, 9901–9904 (2000).

Acknowledgements

We acknowledge support from European Union's Horizon 2020 Research and Innovation programme (GrapheneCore3 881603, LIGHT-CAP 101017821, GREENCAP 101091572, X.F.), M-ERA.NET and Sächsisches Staatsministerium für Wissenschaft und Kunst (HYSUCAP 100478697, E.Z., T.Š., X.F.), and the German Research Foundation (DFG, CRC1415, grant number 417590517, E.B., M.Y., X.F.). TAČR EPSILON

project (number TH71020004, T.Š.), GAČR project (number 23-07617S, T.Š.) and CzechNanoLab project (number LM2023051, T.Š.) funded by MEYS CR are gratefully acknowledged for the financial support of the measurements in the CEITEC Nano Research Infrastructure. D.B. acknowledges support of computational resources in Mons by the FNRS 'Consortium des Equipements de Calcul Intensif–CECI' programme (grant number 2.5020.11) and by the Walloon Region (ZENOBE Tier-1 supercomputer, 1117545). D.L. acknowledges support from the China Scholarships Council (CSC). P.P.M. was supported by the National Science Centre (project number 2018/31/D/ST5/00399) and the National Centre for Research and Development (project number LIDER/8/0055/L-12/20/NCBR/2021). The authors acknowledge the use of the facilities at the Dresden Center for Nanoanalysis (DCN), Technische Universität Dresden, the Gemeinsamen Wissenschaftskonferenz (GWK) support for providing computing time through the Center for Information Services and High-Performance Computing (ZIH) at TU Dresden, and beam-time allocation at beamline P65 of the PETRA III synchrotron (DESY, Hamburg, Germany) and beamline BL04 of the ALBA synchrotron (Barcelona, Spain). We specially thank S. Voborný, P. Jadhao and P. Chen for helpful discussions.

Author contributions

M.Y. and X.F. conceived and supervised the research. D.L. performed most of the experiments and analysis. W.Z., H.I.W. and M.B. performed the THz spectra test and analysis. S.M.G. and D.B. implemented the theoretical calculations. K.S., M.H., M.D., E.Z. and T.Š. conducted the transmission electron microscopy test and analysis. J.P. performed the XPS test. P.P.M. carried out the SIMS test. N.L. and E.B. conducted the solid-state NMR test. Z.L. and S.Z. carried out the electrical conductivity test. J.Z. assisted with XAS experiment. D.S. assisted with electrochemical experiments. D.L. prepared the paper under the supervision of M.Y. and X.F. All the authors read and revised the paper.

Competing interests

The authors declare no competing interests.

Additional information

Supplementary information The online version contains supplementary material available at https://doi.org/10.1038/s41563-024-01911-2.

Correspondence and requests for materials should be addressed to Hai I. Wang, David Beljonne, Minghao Yu or Xinliang Feng.

Peer review information *Nature Materials* thanks Michel Barsoum, Qing Huang and the other, anonymous, reviewer(s) for their contribution to the peer review of this work.